In-medium modifications of open and hidden strange-charm mesons from spatial correlation functions

A. Bazavov,[1] F. Karsch,[2,3] Y. Maezawa,[2] Swagato Mukherjee,[3] and P. Petreczky[3]

[1]*Department of Physics and Astronomy, University of Iowa, Iowa City, Iowa 52240, USA*
[2]*Fakultät für Physik, Universität Bielefeld, D-33615 Bielefeld, Germany*
[3]*Physics Department, Brookhaven National Laboratory, Upton, New York 11973, USA*

We calculate spatial correlation functions of in-medium mesons consisting of strange-antistrange, strange-anticharm and charm-anticharm quarks in $(2 + 1)$-flavor lattice QCD using the highly improved staggered quark action. A comparative study of the in-medium modifications of mesons with different flavor contents is performed. We observe significant in-medium modifications for the ϕ and D_s meson channels already at temperatures around the chiral crossover region. On the other hand, for the J/ψ and η_c meson channels in-medium modifications remain relatively small around the chiral crossover region and become significant only above 1.3 times the chiral crossover temperature.

I. INTRODUCTION

At high temperatures matter controlled by the strong force undergoes a chiral crossover transition [1], accompanied by the deconfinement of flavor quantum numbers carrying degrees of freedom [2]. The relevant degrees of freedom change from hadrons to quarks and gluons (see e.g. Refs. [3,4] for recent reviews). The in-medium modification and dissolution of heavy quarkonium were suggested as a signal for creating a deconfined medium in heavy ion collisions by Matsui and Satz [5]. The existence of heavy-light mesons above the chiral transition temperature has also been proposed to explain the large energy loss and flow of heavy quarks observed in heavy ion collisions [6]. Recent lattice QCD calculations suggest that heavy-light bound states dissolve already at or close to the QCD transition temperature based on flavor and quantum number correlation analysis [7].

Hadronic correlation functions have long been advocated as convenient tools to explore the properties of strong interaction matter [8,9]. They encode the in-medium properties of hadrons, as well as their dissolution. Moreover, through the comparison of lattice results with weak coupling calculations at high temperature [10,11] they also provide information on the change from strongly to weakly interacting matter.

Spectral functions, the Fourier transforms of real time meson correlation function, are the basic quantities that provide knowledge regarding the in-medium properties of mesons and their dissolution. Meson states appear as peaks in the corresponding spectral functions with the peak position equal to the meson mass. The width of the peak corresponds to the in-medium width of the meson. However, lattice QCD is formulated in Euclidean space time. Temporal meson correlation functions calculated on the lattice,

$$G(\tau, \vec{p}, T) = \int d^3x e^{i\vec{p}\cdot\vec{x}} \langle J_H(\tau, \vec{x}) J_H(0, \vec{0}) \rangle, \quad (1)$$

have a simple relation to the spectral function, $\sigma(\omega, \vec{p}, T)$:

$$G(\tau, \vec{p}, T) = \int_0^\infty d\omega \sigma(\omega, \vec{p}, T) K(\omega, \tau, T),$$
$$K(\omega, \tau, T) = \frac{\cosh(\omega(\tau - 1/2T))}{\sinh(\omega/2T)}. \quad (2)$$

Here J_H is a meson operator, typically of the form $J_H = \bar{q}\Gamma_H q$, with Γ_H being some combination of the Dirac matrices that specifies the quantum numbers of the meson. One way to obtain the spectral function from the above relation is to use the maximum entropy method [12–19]. The analysis of temporal correlation functions is difficult due to the limited extent, $1/T$, in the Euclidean time direction. In the case of heavy quarkonium correlators, for instance, it turned out that the melting of bound states does not lead to large changes in the correlation functions [19,20]. In order to become sensitive to the corresponding disappearance of a resonance peak in the spectral function high statistical accuracy and the analysis of the correlation function at a large number of Euclidean time separations are needed. At fixed temperature $T = 1/N_\tau a$, this requires large lattices with the temporal extent N_τ and sufficiently small lattice spacing, a.

Alternatively, one can study the spatial correlation functions of mesons

$$G(z, T) = \int_0^{1/T} d\tau \int dx dy \langle J_H(\tau, x, y, z) J_H(0, 0, 0, 0) \rangle. \quad (3)$$

These are related to the spectral functions in a more complicated way that also involves integration of momenta,

$$G(z,T) = \int_0^\infty \frac{2d\omega}{\omega} \int_{-\infty}^\infty dp_z e^{ip_z z} \sigma(\omega, p_z, T). \quad (4)$$

Since the spatial separation is not limited by the inverse temperature, the spatial correlation function can be studied at separations larger than $1/T$. Therefore, the spatial correlation functions can be more sensitive to in-medium modifications and/or the dissolution of mesons. Another advantage of spatial correlation functions over the temporal ones is that the spatial correlation function can be directly compared to the corresponding vacuum correlation function to quantify modifications of the in-medium spectral function. It is apparent from Eq. (2) that for the temporal correlation function the temperature dependent in-medium modifications of the spectral function are partly masked by the temperature dependence of the kernel $K(\omega, \tau, T)$, and a comparison with the corresponding vacuum correlation function demands evaluation of the reconstructed correlator [16]. Such a complication is not present for the spatial correlation functions.

While the general relation between spectral functions and spatial meson correlators is more involved, in some limiting cases it becomes simple. At large distances the spatial correlation functions decay exponentially, $G(z,T) \sim \exp(-M(T)z)$, where M is known as the *screening mass*. Note that, unlike the in-medium temporal correlation functions, the transport contributions to the spectral functions at small frequencies do not lead to a nondecaying constant in the large distance behavior of the spatial correlation functions. At small enough temperatures when there exists a well-defined mesonic bound state, the spectral function has the form $\sigma(\omega, 0, 0, p_z, T) \sim \delta(\omega^2 - p_z^2 - m_0^2)$, and M becomes equal to the (pole) mass m_0 of the meson. On the other hand, at high enough temperatures, when the mesonic excitations are completely melted, the spatial meson correlation functions describe the propagation of a free quark-antiquark pair. The screening masses are then given by [21]

$$M_{\text{free}} = \sqrt{m_{q_1}^2 + (\pi T)^2} + \sqrt{m_{q_2}^2 + (\pi T)^2}, \quad (5)$$

where m_{q_1} and m_{q_2} are the masses of the quark and antiquark that form the meson. This form of the screening mass in the noninteracting limit is a direct consequence of the antiperiodic boundary conditions in Euclidean time that are needed for the representation of fermions at nonzero temperature. This leads to the appearance of a smallest nonzero Matsubara frequency, πT, in the quark and antiquark propagators. As the bosonic meson state is dissolved in the noninteracting limit the screening mass results as the contribution of two independently propagating fermionic degrees of freedom. Thus the transition between these two limiting values of the screening mass can be used as an indicator for the thermal modification and eventual dissolution of mesonic excitations.

Lattice QCD studies of the screening masses of light quark mesons have been performed within the quenched approximation [22,23] and also with two dynamical flavors using staggered [24] as well as Wilson-type quarks [25]. Screening masses in the light and strange quark sector have been studied recently in $(2 + 1)$-flavor QCD using the so-called $p4$ staggered fermion action [26,27] and the expected qualitative behavior discussed above was observed. Furthermore, the study has been extended to the case of charmonium providing the first direct evidence for melting of the charmonium ground state [28] from lattice QCD with light dynamical quark degrees of freedom.

In this work we report, for the first time, on studies of spatial meson correlators and screening masses using the highly improved staggered quark (HISQ) action [29] with a strange quark mass tuned to its physical value and almost physical, degenerate up and down quark masses. The HISQ action is known to lead to discretization effects that are smaller than those observed with all other staggered-type actions currently used in studies of lattice QCD thermodynamics [30]. Moreover, the HISQ action is well suited to study heavy quarks on the lattice [29] and turned out to be successful in quantitative studies of charmonium [31] and D meson properties [32]. In this work we study the spatial correlation functions of mesonic excitations with strange (s) and charm (c) quarks, specifically the lowest states in the pseudoscalar, vector, scalar and axial vector channels for the $s\bar{s}$, $s\bar{c}$ and $c\bar{c}$ flavor combinations. In the following we refer to the meson states corresponding to these flavor combinations as hidden strange, open charm-strange and hidden charm mesons. Some preliminary results from this study have been published in conference proceedings [33,34].

II. LATTICE SETUP

We calculate meson correlation functions on gauge configurations generated in $(2 + 1)$-flavor QCD using the HISQ action [30]. The strange quark mass m_s is adjusted to its physical value and the light quark masses are fixed at $m_l = m_s/20$, corresponding to $m_\pi \simeq 160$ MeV and $m_K \simeq 504$ MeV at zero temperature in the continuum limit [30]. Charm quarks are introduced as valance quarks and we use the HISQ action with the so-called ϵ-term for the charm quark mass [29] which makes our calculations in the heavy quark sector free of tree-level discretization errors up to $\mathcal{O}((am_c)^4)$. Our calculations have been performed on lattices of the size $N_\sigma^3 \times N_\tau = 48^3 \times 12$. We consider lattice couplings in the range $\beta = 6.664$–7.280 which correspond to temperatures $T = 138$–248 MeV. This enables investigation of in-medium modifications of meson properties below and above the chiral crossover transition at $T_c = (154 \pm 9)$ MeV [30]. To study the spatial correlators at higher temperatures we adopt the

fixed-scale approach and perform calculations at $\beta = 7.280$ for $N_\tau = 10, 8, 6, 4$, which corresponds to the temperature range $T = 298$–744 MeV. In all our calculations the spatial extent of the lattice is four times the temporal extent: $N_\sigma = 4N_\tau$. The lattice spacing and the resulting temperature values, $T = 1/N_\tau a$, have been determined using results for the kaon decay constant [30]. These temperatures together with the run parameters for all our finite temperature calculations are summarized in Table I.

In the staggered formulation quarks come in four valence tastes and meson operators are defined as $J_H = \bar{q}(\Gamma^D \times \Gamma^F)q$, Γ^D and Γ^F being products of Dirac gamma matrices which generate spin and taste structures, respectively [35]. In this study we focus only on local meson operators with $\Gamma^D = \Gamma^F = \Gamma$. By using staggered quark fields $\chi(\boldsymbol{x})$ at $\boldsymbol{x} = (\tau, x, y, z)$ the local meson operators can be written in a simple form $J_H(\boldsymbol{x}) = \tilde{\phi}(\boldsymbol{x})\bar{\chi}(\boldsymbol{x})\chi(\boldsymbol{x})$, where $\tilde{\phi}(\boldsymbol{x})$ is a phase factor depending on the choice of Γ. We calculate only the quark-line connected part of the meson correlators since the contribution of the disconnected part either vanishes or is expected to be small in most cases considered in this study (see discussions below). Since a staggered meson correlator couples to two different meson excitations with opposite parity, the large distance behavior of the lattice correlator can be described by

$$G(\tau) = A_{NO}^2(e^{-M_-\tau} + e^{-M_-(N_\tau - \tau)})$$
$$- (-1)^\tau A_O^2(e^{-M_+\tau} + e^{-M_+(N_\tau - \tau)}), \quad (6)$$

where the first (second) term on the right-hand side characterizes a nonoscillating (oscillating) contribution governed by a negative (positive) parity state. Taking the square of the amplitudes ensures their positivity [36]. In Table II we summarize the different choices of the phase factor $\tilde{\phi}$ and the meson states they correspond to. We have considered four channels, which we denote as scalar (S), pseudoscalar (PS), axial vector (AV) and vector (V). Notice that the oscillating state does not exist for the PS channel of $s\bar{s}$ and $c\bar{c}$ sectors [35], thus we impose $A_O = 0$ on these correlators. The negative parity states in these channels correspond to different tastes of the same physical meson and will thus have nearly degenerate masses if lattice spacing is sufficiently small. For instance, in the $c\bar{c}$ sector the negative parity states in S and PS channels both correspond to the same η_c state. We will comment on this in more detail later.

In Eq. (6) as well as in Table II we assume that the direction of propagation is the imaginary time τ. When discussing spatial correlation functions we assume that the direction of propagation is z. In that case, z should be replaced by τ in Table II and τ and N_τ should be replaced by z and N_σ in Eq. (6), respectively. We calculate meson propagators using point sources as well as corner-wall sources, where on a given time slice the source is set to one at the origin of each 2^3 cube and zero elsewhere. The use of corner-wall sources reduces the contribution of higher excited states and thus allows for a more accurate determination of the screening masses, especially for the positive parity states.

TABLE I. Gauge coupling (β), strange (m_s) and charm (m_c) quark masses, temporal lattice sizes (N_τ) and the number of trajectories (traj.) used for the finite temperature calculations. The light quark mass is fixed as $m_l = m_s/20$. The meson correlation functions are calculated every ten trajectories. The spatial lattice extent is $N_\sigma = 4N_\tau$. We also show the temperature values determined using f_K as an input.

β	am_s	am_c	N_τ	traj.	T [MeV]
6.664	0.0514	0.632	12	3740	138.2
6.700	0.0496	0.604	12	6500	143.3
6.740	0.0476	0.575	12	6170	149.0
6.770	0.0460	0.554	12	6320	153.5
6.800	0.0448	0.534	12	6590	158.0
6.840	0.0430	0.509	12	7910	164.3
6.860	0.0420	0.497	12	3660	167.5
6.880	0.0412	0.486	12	9620	170.8
6.910	0.0400	0.469	12	4130	175.8
6.950	0.0386	0.448	12	6200	182.6
6.990	0.0370	0.429	12	5100	189.6
7.030	0.0356	0.410	12	6700	196.9
7.100	0.0332	0.380	12	10050	210.2
7.150	0.0320	0.360	12	9590	220.2
7.280	0.0284	0.315	12	11120	247.9
7.280	0.0284	0.315	10	4180	297.5
7.280	0.0284	0.315	8	4990	371.9
7.280	0.0284	0.315	6	3810	495.8
7.280	0.0284	0.315	4	4820	743.7

TABLE II. List of meson operators and corresponding physical states in the strange ($s\bar{s}$), strange-charm ($s\bar{c}$) and charm ($c\bar{c}$) sectors. The lightest $s\bar{s}$ pseudoscalar state is defined as $M_{\eta_{s\bar{s}}} = \sqrt{2M_K^2 - M_\pi^2} \sim 686$ MeV which is used to determine the strange quark mass on the zero-temperature lattices.

	$-\tilde{\phi}(x)$	Γ	J^{PC}	$s\bar{s}$	$s\bar{c}$	$c\bar{c}$
M_-^S		$\gamma_4\gamma_5$	0^{-+}	$\eta_{s\bar{s}}$	D_s	η_c
	1					
M_+^S		1	0^{++}		D_{s0}^*	χ_{c0}
M_-^{PS}		γ_5	0^{-+}	$\eta_{s\bar{s}}$	D_s	η_c
	$(-1)^{x+y+z}$					
M_+^{PS}		γ_4	0^{+-}	$-$		$-$
M_-^{AV}		$\gamma_i\gamma_4$	1^{--}	ϕ	D_s^*	J/ψ
	$(-1)^x, (-1)^y$					
M_+^{AV}		$\gamma_i\gamma_5$	1^{++}	$f_1(1420)$	D_{s1}	χ_{c1}
M_-^V		γ_i	1^{--}	ϕ	D_s^*	J/ψ
	$(-1)^{x+z}, (-1)^{y+z}$					
M_+^V		$\gamma_j\gamma_k$	1^{+-}			h_c

As stated above, in this study we do not include the contribution from disconnected diagrams. In the case of charmonium the contribution of disconnected diagrams is expected to be small, see e.g. Ref. [37]. For $s\bar{s}$ mesons disconnected diagrams will cause mixing with the light quark sector in the isospin zero channel. For vector mesons this mixing is known to be very small and the ϕ meson is almost a pure $s\bar{s}$ state. In SU(3) quark model language this is called the ideal mixing between SU(3) flavor singlet and SU(3) flavor octet. Thus, neglecting the disconnected diagrams also seems to be justified in this case. Mixing is, however, large for isosinglet pseudoscalar mesons. For a realistic study of η and η' mesons it is certainly necessary to include contributions from disconnected diagrams. Thus, we do not pursue a detailed study of the pseudoscalar meson correlators in the $s\bar{s}$ sector. It is customary, however, to compare the lattice calculations of the pseudoscalar meson mass which do not include disconnected diagrams with the mass of the fictitious unmixed $s\bar{s}$ meson that is estimated using leading order chiral perturbation theory $m_{\eta_{s\bar{s}}} = \sqrt{2m_K^2 - m_\pi^2} = 686$ MeV, with m_K and m_π being the kaon and pion masses, respectively. We will use this approach in what follows.

Not much is known about the mixing between the light and strange sectors for isoscalar mesons in scalar and axial vector channels. It is expected that there is strong mixing in the scalar meson sector as well. The mass of the lowest lying $s\bar{s}$ scalar meson considered in our calculation is about 1.12 GeV, as shown in Fig. 1 (explained below). It is considerably heavier than the lightest isoscalar scalar meson $f_0(980)$ but lighter than the next-to-lightest
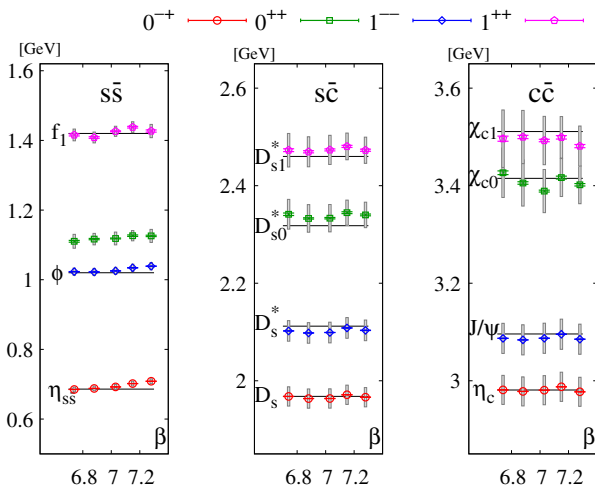
isoscalar scalar state $f_0(1370)$. However, for the axial vector meson mass we find good agreement between our calculations and the mass of the $f_1(1420)$ meson, suggesting that the mixing between the light and strange quark sector is likely to be small in this case. Thus, in the strange sector we could study reliably the correlators in the vector and axial vector channels. Moreover, at sufficiently high temperatures we expect that the contribution of disconnected diagrams will become small because of screening effects and the weakly interacting nature of the deconfined phase. Even in the pseudoscalar channel our calculations will therefore be reliable for high enough temperatures.

III. ZERO-TEMPERATURE CALCULATIONS AND DETERMINATION OF CHARM QUARK MASS

Before discussing our results on the temperature dependence of the spatial correlators and the screening masses we need to determine the charm quark mass at the various values of the gauge coupling used in our finite temperature calculations and understand the accuracy that is reachable in our approach. For this purpose we analyze the meson spectrum at zero temperature at five values of the gauge couplings spread over the range of couplings used in our finite temperature calculations. The run parameters for these calculations are summarized in Table III.

For the determination of the charm quark mass we calculate the masses of J/ψ and η_c mesons for gauge couplings $\beta = 10/g^2$ in the interval $[6.39, 7.28]$. We calculate correlation functions at several trial values of the bare charm quark mass in the range $10 \leq m_c/m_s \leq 14$ using point sources. We then perform linear interpolations in the charm quark mass of the spin-averaged charmonium mass, $(m_{\eta_c} + 3m_{J/\psi})/4$, and match them to the physical value. This determines the bare charm quark mass am_c and the quark mass ratio m_c/m_s for each value of β. Finally we fit the β dependence of am_c to a renormalization group inspired ansatz,

$$am_c^{\text{LCP}} = \frac{c_0 f(\beta) + c_2(10/\beta)f^3(\beta)}{1 + d_2(10/\beta)f^2(\beta)}, \qquad (7)$$

FIG. 1 (color online).   Zero-temperature masses of the lowest lying $s\bar{s}$, $s\bar{c}$ and $c\bar{c}$ mesons. Corresponding experimental values are depicted by the horizontal lines. The error bars and broad gray bands indicate the statistical and systematic errors, respectively. The systematic errors also include the scale uncertainty (see text). In the $s\bar{s}$ sector we compare our results with the mass of the unmixed $\eta_{s\bar{s}}$ pseudoscalar meson (see text).

TABLE III.   Gauge coupling (β), strange (m_s) and charm (m_c) quark masses, lattice sizes ($N_\sigma^3 \times N_\tau$) and the number of trajectories (traj.) used for our zero-temperature spectrum calculations. The light quark mass is fixed $m_l = m_s/20$. The meson correlation functions are calculated every five (six) trajectories for $N_\tau = 48$ (64).

β	am_s	am_c	$N_\sigma^3 \times N_\tau$	traj.
6.740	0.0476	0.575	48^4	5995
6.880	0.0412	0.486	48^4	5995
7.030	0.0356	0.410	48^4	6995
7.150	0.0320	0.360	$48^3 \times 64$	6096
7.280	0.0284	0.315	$48^3 \times 64$	6096

$$f(\beta) = \left(\frac{10b_0}{\beta}\right)^{-b_1/(2b_0^2)} \exp\left(-\frac{\beta}{20b_0}\right), \qquad (8)$$

where b_0 and b_1 are the coefficients of the QCD beta function. The above formula defines the line of constant physics for the charm quark mass. From our fit we find $c_0 = 61.0(1.7)$, $c_2 = 2.76(26) \times 10^5$, and $d_2 = 3.3(3.7) \times 10^2$. The details of these calculations are presented in Appendix A.

We performed calculations of meson correlation functions containing a charm quark in four different channels corresponding to local meson operators (see Table II) for $\beta = 6.74, 6.88, 7.03, 7.15$ and 7.28 using point and corner-wall sources. We extract the zero-temperature masses using the ansatz given in Eq. (6). The pseudoscalar and vector meson masses obtained using the corner-wall sources are systematically lower by 0.2% compared to the masses obtained using the point sources. In the case of pseudo-scalar mesons there is also a small difference of about 0.2% or less between the two tastes corresponding to the Goldstone and the lightest non-Goldstone modes. For vector mesons we do not see any statistically significant splitting between states corresponding to different tastes. However, the largest uncertainty in the value of the vector and pseudoscalar masses expressed in physical units arises from the uncertainty in the determination of the lattice spacing through the calculation of the kaon decay constant. This scale setting uncertainty is about 1%.

Our determination of scalar and axial vector meson masses is less accurate due to the fact that we use the simple two-exponential ansatz given in Eq. (6) without including higher excited states. As a result the fit results for the meson masses oscillate as we vary the lower limit τ_{min} of the fit interval. These oscillations persist to all values of τ_{min}, where a reasonable signal can be extracted. To determine the scalar and axial vector meson masses we average over results obtained using different fit intervals, making sure that τ_{min} is large enough that there is no systematic drift in the value of the screening masses beyond these oscillations. The typical difference between the averaged value and the individual fit values of the meson masses is used as an estimate of systematic errors.

Our results for the zero-temperature masses and comparisons with experimental values are shown in Fig. 1. The error bars shown in the figure correspond to the statistical errors. The broad gray bands correspond to the systematic errors due to dependence of our fitted masses on the fit interval and 1% uncertainty of the scale setting discussed above. As one can see from the figure, our calculations reproduce the experimental results within the estimated errors. There is no apparent cutoff dependence of the meson masses in the beta range studied by us. This is partly due to the fact that cutoff dependence of the meson masses is compensated for by the cutoff dependence of the kaon decay constant f_K [38] used to set the lattice spacing.

The deviations of the ϕ and $\eta_{s\bar{s}}$ meson masses from the experimental values at the two highest β are due to the mistuning of the strange quark mass. As discussed in Ref. [39] at $\beta > 7.03$ the values of the strange quark mass are slightly above the nominal value. After retuning the valence strange quark mass to the correct value one indeed finds that the experimental value of the ϕ meson mass is reproduced.

The averaged value of the hyperfine splitting, $m_{J/\Psi} - m_{\eta_c}$, in our calculations turns out to be 107(1) MeV compared to the experimental value of 113.2(7) MeV. The small discrepancy of 6 MeV could be due to the missing contributions from disconnected diagrams, inaccurate tuning of the charm quark mass and slightly larger than the physical light quark mass. Altogether we find that discretization errors in the charm sector are considerably smaller than required for the studies at nonzero temperature that we discuss in the following sections.

IV. TEMPERATURE DEPENDENCE OF SPATIAL MESON CORRELATORS

Having determined the charm quark masses we can perform calculations of the finite temperature $s\bar{s}$, $s\bar{c}$ and $c\bar{c}$ correlation functions in the four different quantum number channels that we have also analyzed at zero temperature.

We start the discussion of our results at nonzero temperature with the temperature dependence of meson correlators. It was pointed out in Ref. [28] that, contrary to the temporal correlation functions, spatial correlation functions show visible changes already in the vicinity of the cross-over temperature even in the case of charmonium. Since staggered meson correlators in each channel contain both negative parity (nonoscillating) and positive parity (oscillating) states, it is important to separate these contributions before studying the temperature dependence of the correlators. As discussed in detail in Appendix B, it is possible to define two separate effective correlators for the negative (nonoscillating, NO) and positive (oscillating, O) parity states of a staggered meson correlation function $G(z)$

$$G_{NO}(z) \equiv A_{NO}^2(z)e^{-M_-(z)z} = \frac{g_1 + g_0 x_+}{x_- + x_+}, \qquad (9a)$$

$$G_O(z) \equiv A_O^2(z)e^{-M_+(z)z} = (-1)^z \frac{g_1 - g_0 x_-}{x_- + x_+}, \qquad (9b)$$

in terms of the local, effective masses, $x_\pm(z) = e^{-M_\pm(z)}$, obtained by solving the equations

$$Ax_\pm^2 \mp Bx_\pm + C = 0. \qquad (10)$$

Here, $A = g_1^2 - g_2 g_0$, $B = g_3 g_0 - g_2 g_1$, $C = g_2^2 - g_3 g_1$ and $g_i \equiv G(z+i)$, $i = 0, 1, 2, 3$, are the values of the meson correlation function at four successive z values. In this
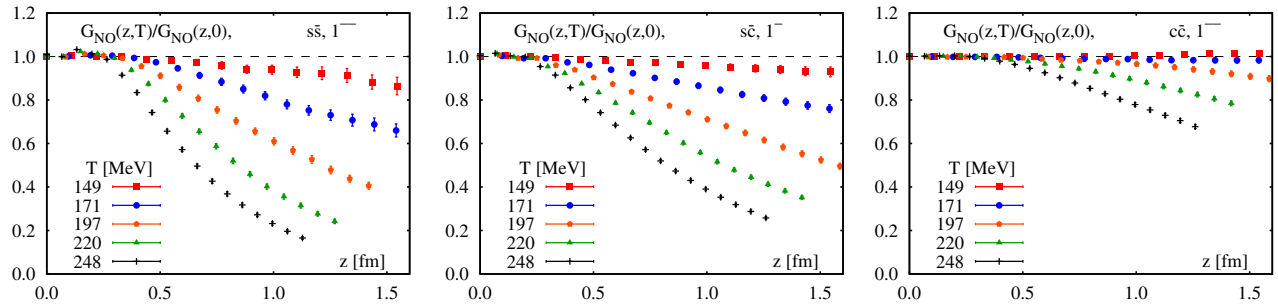
FIG. 2 (color online). Ratios of the nonoscillating (negative parity) part of the vector correlators in $s\bar{s}$ (left), $s\bar{c}$ (middle) and $c\bar{c}$ (right) sectors at different temperatures to the corresponding zero-temperature results. We also show the J^{PC} quantum numbers in each sector. For the D_s meson we have 1^- as there is no charge conjugation symmetry (see Table II).

description we neglect the contribution of the periodic boundary to the propagating direction. Further, one can form ratios of these contributions at different temperatures to the corresponding zero-temperature results. As discussed before, in contrast to temporal correlation functions, such a ratio can directly probe the thermal modifications of the spectral functions themselves. If there is no change in the meson spectral functions, these ratios will be equal to one and deviations from unity will indicate an in-medium modification of the meson spectral functions at nonzero temperature.

In Fig. 2, we show the ratio of the negative parity part of the vector correlator in the $s\bar{s}$, $s\bar{c}$ and $c\bar{c}$ channels to the corresponding zero-temperature correlator, obtained with point sources. At zero temperature, these nonoscillating parts of vector correlators are dominated by the ϕ, D_s^* and J/ψ states, respectively. We show the results only for $z/a < 18$ in the $s\bar{s}$ sector and for $z/a < 20$ in the $s\bar{c}$ and $c\bar{c}$ sectors. At these distances the influence of periodic boundary conditions in the spatial directions can be neglected in the effective meson correlator introduced in Eq. (9). This is discussed in more detail in Appendix B. In the $s\bar{s}$ sector, at large distances, we observe the ~18% and ~38% decrease of this ratio at $T = 149$ and 171 MeV, respectively. A somewhat smaller but still significant ~8% and ~20%, respectively, decrease of this ratio is also seen in the $s\bar{c}$ sector. Note that recent lattice studies based on flavor and quantum number correlations [2,7] have strongly

suggested that open strange and charm mesons already start to melt around $T_c = (154 \pm 9)$ MeV. Thus, a ~20% deviation of the in-medium correlator with respect to the vacuum one depicts a thermally modified spectral function with a melted meson state. For ratios in the J/ψ sector no changes are visible at the lowest 149 MeV temperature, and even at $T = 171$ MeV the deviations of this ratio from unity are at best a few percent. For charmonia the deviations of the in-medium correlators, at large distances with respect to the vacuum ones, become larger than 20% only for $T \gtrsim 200$ MeV. In all cases, the ratio of the correlators decreases with increasing temperature at large distances. As we will see in the next section this is related to the fact that screening masses in the negative parity channels increase with respect to their vacuum values with increasing temperature.

In Fig. 3, we show the ratio of the positive parity (oscillating) part of the axial vector correlator in $s\bar{s}$, $s\bar{c}$ and $c\bar{c}$ channels to the corresponding zero-temperature correlator, again obtained with point sources. We only show the ratio for $z/a < 15$ as at larger distances the effect of periodic boundary conditions cannot be neglected when extracting the positive parity contribution from the correlators (see Appendix B). The meson states that dominate the oscillating part of these correlators are $f_1(1420)$, D_{s1} and χ_{c1}. The ratios of the correlators in this case show a more complex behavior. At a relatively short distance the ratios of the correlators increases, then depending on the
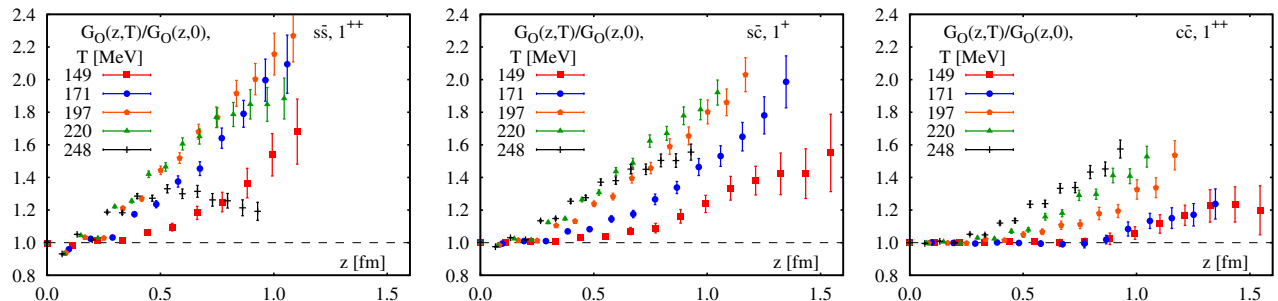

FIG. 3 (color online). Ratios of the oscillating (positive parity) part of axial vector correlators in $s\bar{s}$ (left), $s\bar{c}$ (middle) and $c\bar{c}$ (right) sectors at different temperatures to the corresponding zero-temperature results. See Table II for J^{PC} assignments.

temperature value and the quark content the ratio can also decrease both as a function of z and of the temperature. As will be discussed in the next section, this feature of the correlator ratios is closely related to the behavior of the screening masses of the positive parity states. For not too large temperatures the positive parity screening masses decrease compared to their vacuum values. This corresponds to the increase in the ratio of the correlators at large z. At sufficiently high temperature the screening masses start to increase again, which then leads to the decrease in the ratio of the positive parity correlators. This tendency is seen in the $s\bar{s}$ and $s\bar{c}$ sectors in Fig. 3.

Similar to the case of the negative parity states the size of the medium modification varies with the heavy quark content. It is the largest for $s\bar{s}$ mesons and is the smallest for $c\bar{c}$ mesons. In fact, for charmonium the ratio of the correlators is equal to one for $z < 1$ fm and $T < 171$ MeV, while for the other two cases it is significantly above one already at the lowest temperature. Furthermore, the size of medium modifications of the correlator ratio in the $c\bar{c}$ sector is much larger than for the negative parity part of the vector correlator. This is what one would expect in the sequential charmonium melting picture, where the larger and more loosely bound χ_c states dissolve at a lower temperature than J/ψ.

For the $s\bar{c}$ and $c\bar{c}$ sectors we also consider the pseudoscalar and scalar correlators, as the contributions of the

disconnected diagrams are absent for the former and small for the latter. The results are shown in Fig. 4. The ratios of the nonoscillating part of the pseudoscalar correlators to the corresponding zero-temperature results are shown in the upper panels of Fig. 4. For small temperatures the lowest states that dominate the pseudoscalar correlators are D_s and η_c mesons. The temperature dependence of these ratios is similar to the ratios of the nonoscillating part in the vector channel, i.e. they decrease monotonically with increasing temperatures. For the $c\bar{c}$ case the ratio only shows significant modifications for $T \gtrsim 200$ MeV, while for $s\bar{c}$ sizable modifications are already visible at the lowest temperature. The ratio of the positive parity contribution is shown in the lower panels of Fig. 4, where the corresponding states at $T = 0$ are D_{s0}^* and χ_{c0} for the $s\bar{c}$ and $c\bar{c}$ channels, respectively. The ratio becomes larger than one. In the $c\bar{c}$ sector the deviations of this ratio from one are larger than those in the pseudoscalar case and set in at lower temperatures. Again, these results are suggestive of sequential melting of the charmonia states. The size of medium modifications of the correlator ratio also depends on the heavy quark content: it is larger in the $s\bar{c}$ sector than in the $c\bar{c}$ sector.

The ratio of spatial charmonium correlators and corresponding zero-temperature correlators was first studied in Ref. [28] in the pseudoscalar channel. Strong in-medium modifications of this ratio were found for $zT > 1$.
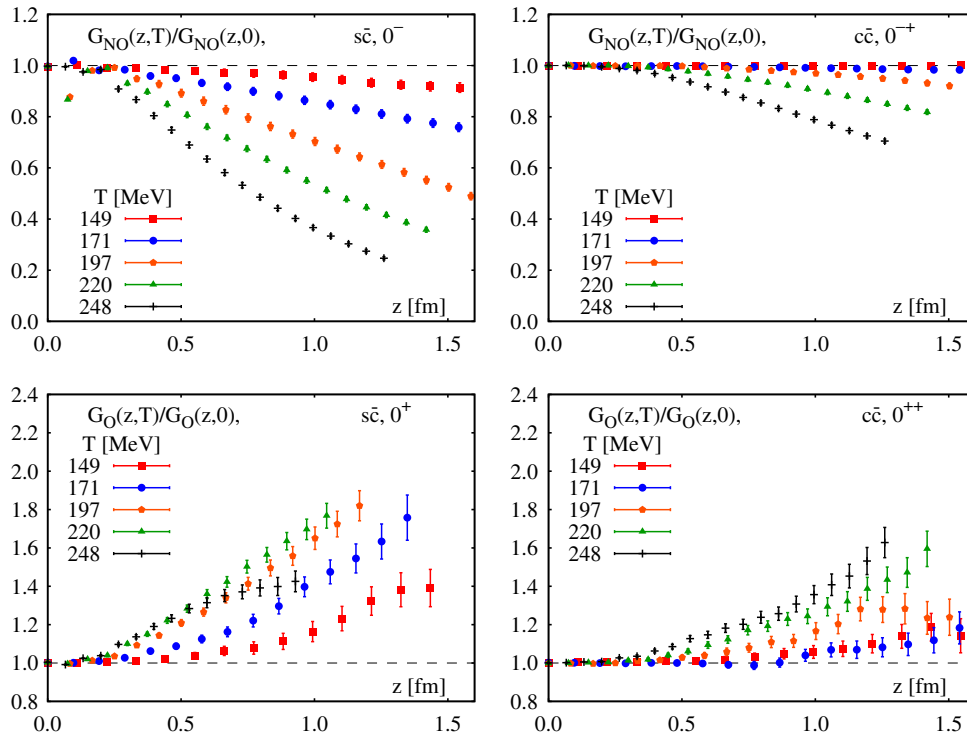

FIG. 4 (color online). Ratios of the nonoscillating (negative parity) part of the pseudoscalar correlators (top panels) and oscillating (positive parity) part of scalar correlators (bottom panels) in $s\bar{c}$ (left panels), and $c\bar{c}$ (right panels) sectors at different temperatures to the corresponding zero-temperature results.

The magnitude of the medium effects in the ratios of pseudoscalar correlators calculated with the HISQ action is similar to that obtained previously with the $p4$ action at the same value of T/T_c. The large changes in the ratio of the spatial correlators, which could be indicative of significant in-medium modification or dissolution of $1S$ charmonium states, are in contrast to the very mild temperature dependence of the analogous ratios of the reconstructed temporal correlators. The reason for this apparent difference lies in the fact that at nonzero temperature the temporal correlators are defined only at relatively small separations $\tau < 1/(2T)$ and, thus, have a limited sensitivity to the in-medium modifications of the spectral functions. As one can see from Figs. 2–4 the medium modification of the spatial correlators for $z < 1/(2T)$ is also quite small. As discussed in Sec. I the access to larger separation is the main reason why the spatial correlation functions are more sensitive to the in-medium modification of the spectral functions.

V. LARGE DISTANCE BEHAVIOR OF SPATIAL MESON CORRELATORS AND SCREENING MASSES

We fit the large distance behavior of the spatial correlators using Eq. (6) and extract screening masses in various channels for $s\bar{s}$, $s\bar{c}$ and $c\bar{c}$ mesons. In our study of PS and V screening masses we use point and corner-wall sources. For the $c\bar{c}$ sector the differences between the results obtained using point and corner-wall sources are quite small. It is typically around 0.4%, except for the three highest temperatures, where it reaches 3%. Similarly in the $s\bar{c}$ sector, the difference between point and corner-wall source results is typically about 1% for all temperatures except the three highest ones, where it is 3%. Larger differences between point and corner-wall source results are seen in the $s\bar{s}$ sector, where they reach 3% at the highest five temperatures, and are about 1% at other temperatures. In the following we will use the results from corner-wall sources when presenting our results on the screening masses in the PS and V channels. In the S and AV channels screening masses can be reliably extracted only by using the corner-wall sources. The effects of taste symmetry breaking are only visible for the negative parity states in PS and S channels at low temperatures, where they are about 1.5%. For temperature above 200 MeV we do not find any statistically significant effects of taste splitting.

All our results on screening masses in the $s\bar{s}$, $s\bar{c}$ and $c\bar{c}$ sectors are summarized in Tables V–VII, respectively, given in Appendix C and are shown in Fig. 5. The error bars in the figure indicate the statistical and systematic errors added in quadrature. We expect that at very high temperature the screening masses are given by Eq. (5). We show the free theory (leading order perturbative) results as dashed lines in Fig. 5. For this we need to specify the quark masses. The quark masses depend on the renormalization scale which is not specified at leading order. A natural
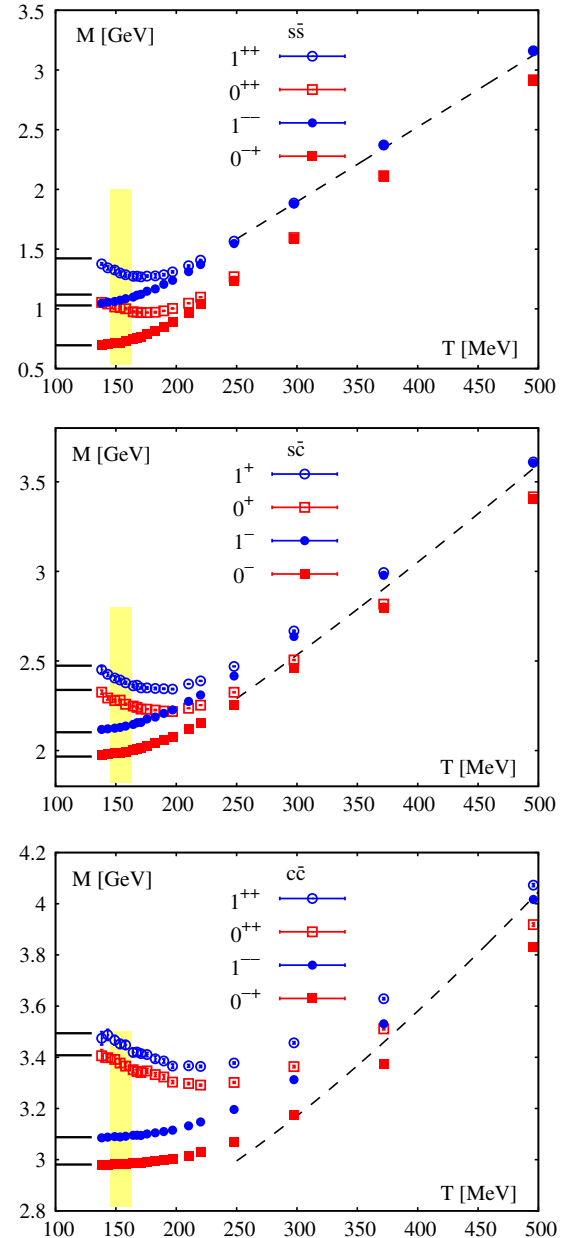

FIG. 5 (color online). Screening masses for different channels in the $s\bar{s}$ (top panel), $s\bar{c}$ (middle panel) and $c\bar{c}$ (bottom panel) sectors as functions of the temperature. The solid horizontal lines on the left depict the corresponding zero-temperature meson masses. The shaded regions indicate the chiral crossover temperature $T_c = (154 \pm 9)$ MeV. The dashed lines are the corresponding free field theory result (see text).

choice of the renormalization scale would be to identify it with the lowest scale in the problem provided that this lowest scale is still in the perturbative region. In our case there are two relevant energy scales, the charm quark mass m_c and the thermal scale, which here is taken to be $2\pi T$. For temperatures $T > 200$ MeV both scales are comparable. Therefore, we could take the charm quark mass as the renormalization scale and the corresponding value

$m_c(\bar{\mu} = m_c) = 1.275$ GeV from the Particle Data Group [40]. Using the renormalization invariant ratio of charm to strange quark mass $m_c/m_s = 11.85$ [41] and the above value, we can determine the value of the strange quark mass at the same renormalization scale to be $m_s = 0.108$ GeV. This completely specifies our free theory prediction.

As one can see from Fig. 5, there are three distinct regions: the low temperature region, where the screening masses are close to the corresponding vacuum masses (the solid lines), the intermediate temperature region, where we see significant changes in the value of the screening masses with respect to the corresponding vacuum masses, and finally, the high temperature region, where the screening masses are close to the free theory result (the dashed lines). In the high temperature region, there clearly are no meson bound states anymore. The onset of the high temperature behavior is different in different sectors. In the $s\bar{s}$ sector it starts at around $T = 210$ MeV. In the $s\bar{c}$ sector it starts at $T = 250$ MeV, while in the $c\bar{c}$ sector it starts at $T > 300$ MeV. As the temperature increases, we see that the screening masses corresponding to negative parity states increase monotonically, while the screening masses in the positive parity states first decrease before starting to rise towards the asymptotic high temperature values. In the intermediate temperature region the screening masses of opposite parity partners start to approach each other and we observe a significant rearrangement of the ordering of screening masses in different channels. At sufficiently high temperatures the PS and S (0^{-+} and 0^{++}) as well as the V and AV (1^{--} and 1^{++}) screening masses become degenerate. In the $s\bar{s}$ sector this is evident for $T > 220$ MeV, while for the two other sectors it happens at higher temperatures due to the larger explicit breaking of parity by the charm quark mass. In the high temperature region the screening masses in the PS channel are smaller than the screening masses in the V channel. This behavior has been observed previously in lattice calculations [26] and in calculations using Dyson-Schwinger equations [42].

In order to emphasize the different behavior of negative and positive parity screening masses in the low and intermediate temperature regions it is convenient to consider the difference between the screening mass and the corresponding vacuum masses m_0 calculated at $T = 0$:

$$\Delta M(T) = M(T) - m_0. \qquad (11)$$

It is tempting to interpret this difference as the change in the binding energy of meson states, however, the relation between the screening mass and the pole mass only holds as long as there is a well-defined bound state. Nonetheless, ΔM could provide some constraints on the change of the binding energy in the low and intermediate temperature regions. We show our results for $\Delta M(T)$ for the vector (1^-) and axial vector (1^+) $s\bar{s}$, $s\bar{c}$ and $c\bar{c}$ mesons in Fig. 6. The error bars and gray bands indicate the statistical and
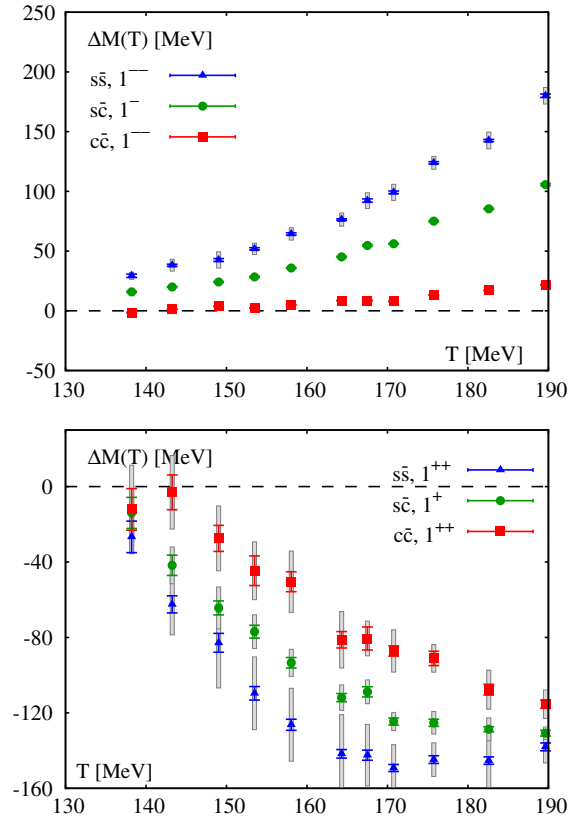

FIG. 6 (color online). The difference, $\Delta M(T) = M(T) - m_0$, of the screening masses, $M(T)$, and the corresponding vacuum masses, m_0, for the negative (top panel) and positive (bottom panel) parity states as functions of the temperature.

systematic errors, respectively. In all cases ΔM increases for negative parity states and decreases for positive parity states in the considered temperature region. This corresponds, of course, directly to the pattern seen in the behavior of ratios of spatial correlation functions (see Figs. 2, 3 and 4). At higher temperatures the positive parity screening masses will start increasing again (see Fig. 5) leading to the nonmonotonic behavior of the correlator ratios in the $s\bar{s}$ and $s\bar{c}$ sectors. Except for the negative parity (S-wave) charmonium states we clearly see that in all other cases in-medium modifications lead to significant deviations of screening masses from pole masses already in the crossover region. In the case of the $s\bar{s}$ states this is the case even below T_c. For the S-wave charmonium states screening and pole masses are nearly compatible up to temperatures of about 200 MeV. This is consistent with the small deviations from unity observed for ratios of zero and finite temperature correlators in these quantum number channels and may indicate that these states do persist as bound states at least up to this value of the temperature. Thus, in the charmonium case the temperature dependence of ΔM provides some hints for sequential thermal modification: It shows a strong decrease of screening masses starting in the crossover region for scalar and

axial vector channels corresponding to $1P$ charmonium states (χ_{c0} and χ_{c1}) and very little change in the pseudo-scalar and vector channels corresponding to $1S$ charmonium states (η_c and J/ψ).

The amplitudes A_{NO}^2 and A_O^2 appearing in Eq. (6) are related to the wave function of meson states and to the meson decay constants (corresponding to weak decays or a decay into a virtual photon) in the zero-temperature limit. In particular, for point sources and mesons consisting of heavy quarks they are proportional to the square of the wave function at the origin and the derivative of the square of the wave function at the origin. As we are interested in signatures for the melting of meson states at high temperatures, it is worth studying the temperature dependence of these amplitudes. In Fig. 7 we show the ratios of the amplitude A_{NO}^2 for the spatial meson correlators in the vector channel to the corresponding zero-temperature result. If meson states exist in the medium with little or no modifications this ratio should be close to one. For the strange and strange-charm mesons we see that there are deviations of this ratio from one already at relatively low temperatures and these deviations are increasing with increasing temperature. For charmonium the ratio of the amplitude to the zero-temperature amplitude is close to one up to a temperature of about 170 MeV, and slowly increases above that temperature. Only at temperatures above 200 MeV are the deviations of this ratio from unity similar to the ones observed in strange and strange-charm sectors in the transition region. This also suggests that significant thermal modifications of the J/ψ occur for $T \gtrsim 200$ MeV.

Finally, we comment on the sensitivity of spatial correlation functions to temporal boundary conditions of the fermionic fields. At finite temperature, the temporal boundary condition must be antiperiodic for the fermionic fields and all gauge field configurations are generated by

imposing such a boundary condition. On the other hand, on these configurations one can measure observables also by imposing periodic temporal boundary conditions for the fermion fields. Such a trick may provide some further insight into the melting of charmonia states [28,43,44]. As discussed above, at asymptotically high temperatures the screening masses approach twice the value of the lowest Matsubara frequency, which arises entirely from the anti-periodic temporal boundary conditions for the fermions. This result reflects that the two fermions (quarks) of the bosonic meson operator propagate independently and are separately sensitive to the antiperiodic boundary conditions. This tells us that if one measures the screening masses of the meson operators by artificially imposing periodic temporal boundary conditions for the fermions, one expects to find vanishing screening masses at very high temperatures. Asymptotically, the quadratic difference of the screening masses calculated with antiperiodic and periodic boundary conditions will approach $(2\pi T)^2$ [28,43,44]. More generally, by comparing the screening masses for mesonic observables calculated with both sets of boundary conditions we can probe to what extent the corresponding correlators are influenced by the boundary conditions, i.e. whether the fermionic substructure of the meson becomes visible and influences the asymptotic behavior of spatial correlation functions. On the other hand, if the two fermions constituting the meson operator remain as a well-defined bosonic bound state, then the corresponding screening mass should be insensitive to the fermionic boundary conditions and we would expect to obtain identical screening masses for both antiperiodic and periodic ones.

In Fig. 8 we show the charmonium screening masses in the pseudoscalar (0^{-+}) and vector (1^{--}) channels
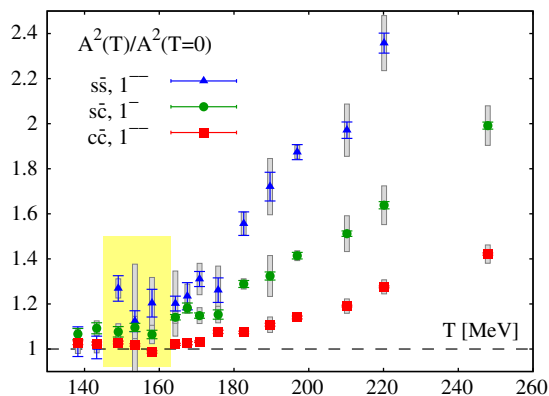

FIG. 7 (color online). The ratio of the amplitude A_{NO}^2 [see Eq. (6)] of the spatial correlators to the corresponding zero-temperature amplitude in the vector channel as a function of the temperature. The shaded region indicates the chiral crossover transition.
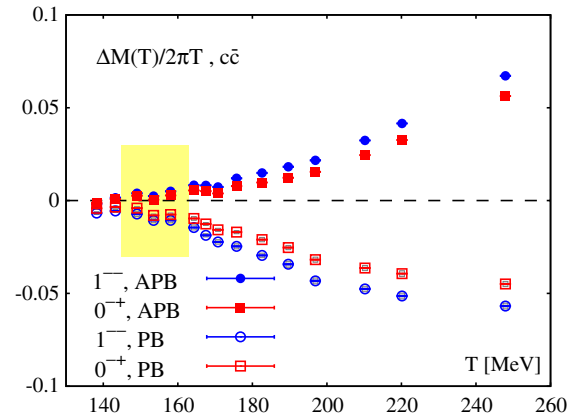

FIG. 8 (color online). The difference, $\Delta M = M(T) - m_0$ normalized by $2\pi T$, between the screening masses and the corresponding zero-temperature masses for the pseudoscalar (0^{-+}) and vector (1^{--}) channels, by imposing the usual antiperiodic (filled symbols) as well as periodic (open symbols) temporal boundary conditions for the fermions (see text). The shaded region shows the chiral crossover transition.

calculated using antiperiodic and periodic boundary conditions. Both channels show similar temperature dependence: Already in the crossover region the screening masses start to become sensitive to the boundary conditions. However, there is little sensitivity to the boundary conditions for $T \lesssim 170$ MeV. Above that temperature we see a clear sensitivity of the screening masses to the boundary conditions which becomes quite large for $T \gtrsim 200$ MeV. This may indicate the dissolution of the η_c and J/ψ states at these temperatures. However, to quantify the "onset temperature" for dissolution is clearly not possible in this way. We also see sensitivity to the boundary conditions in the scalar and axial vector charmonium screening masses. But due to large errors in the corresponding screening masses with the periodic boundary condition it is more difficult to quantify this sensitivity.

VI. CONCLUSIONS

We have studied spatial correlation functions at non-zero temperature for $s\bar{s}$, $s\bar{c}$ and $c\bar{c}$ mesons to investigate their in-medium modifications. We have performed direct comparisons of the in-medium correlation functions with the corresponding zero temperature ones, extracted screening masses and amplitudes from large distance behaviors of the correlation functions and also investigated their sensitivity to the temporal boundary conditions of the charm quark. In all cases, we have found that medium modifications of the spatial meson correlation functions set in the crossover region. However, that the amount of in-medium modifications in the spatial correlators is different in different sectors and decreases with the heavy quark content. The $s\bar{s}$ and $s\bar{c}$ mesons are significantly effected by the medium already at relatively low temperatures and possibly dissolve at temperature close to the crossover temperature, $T_c = (154 \pm 9)$ MeV. For the $c\bar{c}$ mesons, S-wave charmonium states $(J/\psi$ and $\eta_c)$ undergo very small medium modifications up to $T \sim 1.1 T_c$ $(T \sim 170$ MeV) and significant medium modifications are observed only for $T \gtrsim 1.3 T_c$ $(T \gtrsim 200$ MeV). We have also seen a clear difference between the temperature dependence of the correlators corresponding to S-wave charmonium and to P-wave charmonium $(\chi_{c0}$ and $\chi_{c1})$ states. The spatial correlators corresponding to $(\chi_{c0}$ and $\chi_{c1})$ states show sizable medium modifications already in the crossover region. This is in line with the sequential melting of charmonia states—the larger, loosely bound P-wave states dissociate at lower temperatures than the smaller, tightly bound S-wave charmonia.

Let us finally summarize the importance of our findings for the physics of heavy ion collisions. The sequential charmonium melting is an essential ingredient for most of the phenomenological models that attempt to explain charmonium yield in heavy ion collisions. Therefore our findings provide support for these models. The fact that open-charm mesons dissolve at temperatures close to the transition temperature disfavors the models which try to explain the large energy loss of heavy quarks in heavy ion collisions through the existence of heavy-light bound states in quark gluon plasma [6]. Finally the large medium modification of hidden strange meson correlators disfavors scenarios of separate freeze-out of strange degrees of freedom in heavy ion collisions [45].

APPENDIX A: DETERMINATION OF CHARM QUARK MASS

Here we determine the line of constant physics (LCP) for the charm quark mass. To estimate the charm quark mass, we calculate the masses of the negative parity ground states, $J^{PC} = 0^{-+}$ and 1^{--}, which correspond to the η_c and J/ψ mesons, respectively, in a range of couplings $\beta = 6.39$–7.28 with several trial values for the ratio of the bare charm to strange quark masses, m_c/m_s, using point sources. We summarize the simulation parameters and lattice sizes

TABLE IV. The gauge couplings (β), lattice sizes ($N_\sigma^3 \times N_\tau$) and strange quark mass (m_s) used to determine the charm quark mass. Results of the ratio of charm and strange quark masses $(m_c/m_s)_{\rm LCP}$ and the charm quark mass $am_c^{\rm LCP}$ on the line of constant physics are also summarized.

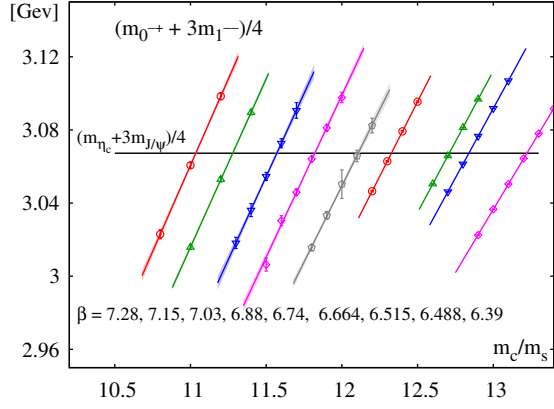| β	$N_\sigma^3 \times N_\tau$	am_s	$(m_c/m_s)_{\rm LCP}$	$am_c^{\rm LCP}$
6.390	32^4	0.0694	13.2222(40)	0.91762(27)
6.488	32^4	0.0620	12.8386(33)	0.79600(21)
6.515	32^4	0.0604	12.7091(54)	0.76763(33)
6.664	32^4	0.0514	12.327(12)	0.63361(66)
6.740	48^4	0.0476	12.107(13)	0.57631(62)
6.880	48^4	0.0412	11.8208(53)	0.48702(22)
7.030	48^4	0.0356	11.5702(85)	0.41190(30)
7.150	$48^3 \times 64$	0.0320	11.2789(43)	0.36092(14)
7.280	$48^3 \times 64$	0.0284	11.0350(55)	0.31339(15)

FIG. 9 (color online). Results for the spin-averaged charmonium mass $(m_{0^{-+}} + 3m_{1^{--}})/4$ for several trial m_c/m_s values of each β. The charm quark mass on LCP is determined by matching those to the physical value $(m_{\eta_c} + 3m_{J/\psi})/4$, summarized in Table IV.

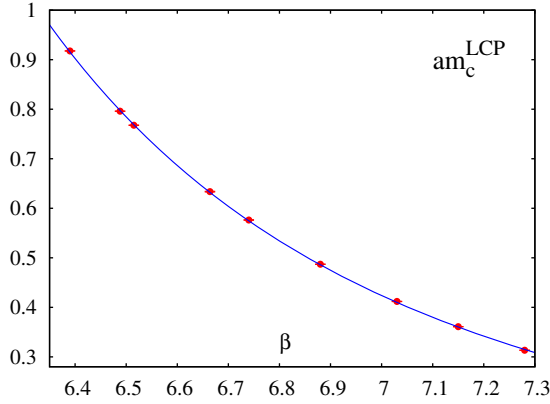

FIG. 10 (color online). Results for the charm quark mass on LCP as a function of β. The curve shows the fit result (see text).

in Table IV, and show results for the spin-averaged charmonium mass $(m_{0^{-+}} + 3m_{1^{--}})/4$ as a function of m_c/m_s for each β in Fig. 9. In the figure, we interpolate the masses linearly for each β and estimate the line of constant physics for the ratio $(m_c/m_s)_{\text{LCP}}$ from the intersection with the physical value $(m_{\eta_c} + 3m_{J/\psi})/4$. The numerical results are also summarized in Table IV.

From the ratio $(m_c/m_s)_{\text{LCP}}$ we determine the charm quark mass on LCP shown in Fig. 10. We fit the data with the renormalization group inspired by Eq. (7) and obtain $c_0 = 61.0(1.7)$, $c_2 = 2.76(26) \times 10^5$ and $d_2 = 3.3(3.7) \times 10^2$. The fit result is also shown in Fig. 10 as a solid curve.

APPENDIX B: NEGATIVE AND POSITIVE PARITY PARTS OF STAGGERED MESON CORRELATOR FROM EFFECTIVE MASSES

In this appendix we briefly discuss our procedure for identifying separate contributions of the negative

(nonoscillating) and positive (oscillating) parity states in a given staggered meson correlation function.

We assume that the staggered meson correlator can be described by a single negative and a single positive parity meson state:

$$G(z) = A_{NO}^2(z)e^{-M_-(z)z} - (-1)^z A_O^2(z)e^{-M_+(z)z}. \quad \text{(B1)}$$

For simplicity, contributions arising from the periodicity of the lattice in the z direction have been neglected. Thus, the correlator is parametrized by four quantities: A_{NO}, A_O and $M_\pm$. Assuming that, for a given value of z, these four parameters vary little over at least four successive points in z, one can determine the parameters from values of the correlation function at these four points: $g_i \equiv G(z + i)$ with $i = 0$, 1, 2, 3. With $x_\pm \equiv e^{-M_\pm}$ and the assumption $x_+ \neq x_-$, it is easy to see

$$\frac{g_{i+2} - g_{i+1}x_-}{g_{i+1} - g_i x_-} = -x_+, \quad \text{for } i = 0, 1, \quad \text{(B2)}$$

yielding a quadratic equation for x_-:

$$(g_2 - g_1 x_-)^2 = (g_3 - g_2 x_-)(g_1 - g_0 x_-). \quad \text{(B3)}$$

Similarly, one can obtain a quadratic equation for x_+

$$(g_2 + g_1 x_+)^2 = (g_3 + g_2 x_+)(g_1 + g_0 x_+). \quad \text{(B4)}$$

Both equations can be expressed in simple quadratic equations,

$$Ax_\pm^2 \mp Bx_\pm + C = 0, \quad \text{(B5)}$$

where $A = g_1^2 - g_2 g_0$, $B = g_3 g_0 - g_2 g_1$ and $C = g_2^2 - g_3 g_1$. Under a condition $A \cdot C < 0$, definite solutions are given by

$$x_\pm = \pm \frac{B}{2A} + \frac{\sqrt{B^2 - 4AC}}{2|A|}. \quad \text{(B6)}$$

Once the local, effective masses $x_\pm$ are determined, it is possible to define two separate effective correlators for the negative (nonoscillating) and positive (oscillating) parity states of a staggered meson correlation function:

$$G_{NO}(z) \equiv A_{NO}^2(z)e^{-M_-(z)z} = \frac{g_1 + g_0 x_+}{x_- + x_+}, \quad \text{(B7a)}$$

$$G_O(z) \equiv A_O^2(z)e^{-M_+(z)z} = (-1)^z \frac{g_1 - g_0 x_-}{x_- + x_+}. \quad \text{(B7b)}$$

As an illustrative example, in Fig. 11 we show the local, effective masses, $M_\pm = -\ln x_\pm$, obtained from the point source correlator of $c\bar{c}$ scalar channel at $T = 248$ MeV as a function of z. At $T = 0$ the positive parity 0^{++} (negative parity 0^{-+}) state corresponds to χ_{c0} (the different taste of
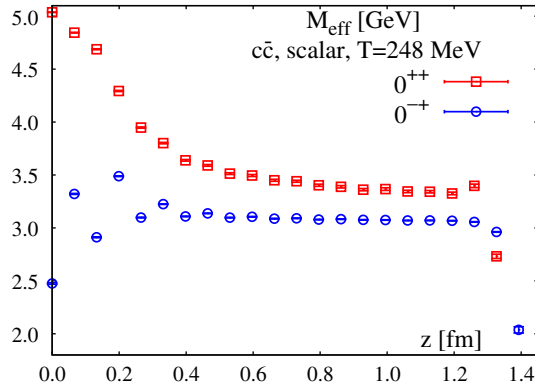
FIG. 11 (color online). Effective masses of the negative (0^{-+}) and positive (0^{++}) parity states, as functions of distance, for the $c\bar{c}$ scalar channel at $T = 248$ MeV.
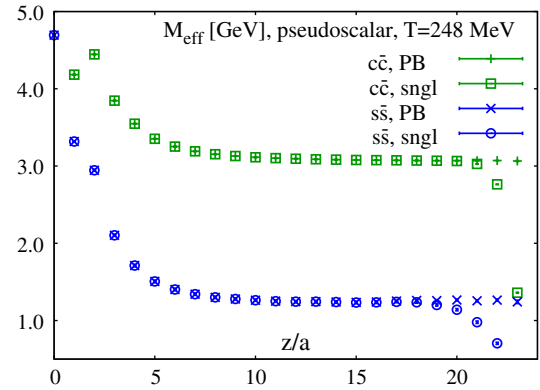

FIG. 12 (color online). The effective masses for the $s\bar{s}$ and $c\bar{c}$ pseudoscalar channel at $T = 248$ MeV as functions of distance, obtained by including the effects of periodicity in the z direction (PB) and also by using a single exponential decay ansatz (sngl).

η_c). The effective masses for different parity states can be well identified in this way, and plateaus appear at $z \geq$ 0.5 fm for the negative parity state and at $z \geq 0.8$ fm for the positive parity state. At large distances, $z \geq 1.2$ fm, the plateaus get worse due to the periodicity in the z direction.

To estimate systematic errors that arise from neglecting the periodic terms in Eq. (B1) it is easier to look into the pseudoscalar correlators in the $s\bar{s}$ and $c\bar{c}$ sectors, as they do not receive a contribution from an oscillating state. In this case, the correlation function is parametrized as

$$G(z) = A_{NO}^2(z)[e^{-M_-(z)z} + e^{-M_-(z)(N_z - z)}]. \quad (B8)$$

The second term on the right-hand side arises from the periodic boundary conditions in the z direction. If one neglects the periodicity, the effective mass is simply obtained from the single exponential decay (sngl) form,

$$M_-^{\text{sngl}}(z) = \ln \frac{G(z)}{G(z+1)}. \quad (B9)$$

On the other hand, the effective mass including the effects of periodic boundary (PB) can be determined from the numerical solution of the equation

$$f(M^{\text{PB}}) \equiv \frac{\cosh[M_-^{\text{PB}}(z)(z - \frac{N_z}{2})]}{\cosh[M_-^{\text{PB}}(z)(z - \frac{N_z}{2} + 1)]} - \frac{G(z)}{G(z+1)} = 0.$$

In Fig. 12 we show results for the effective masses of the $s\bar{s}$ and $c\bar{c}$ pseudoscalar channels at $T = 248$ MeV,

obtained by including the effects of PB as well as using the sngl form. One finds that both effective masses converge at short distances and reach a plateau at moderate values of the distance. At large distances M_-^{PB} stays on the plateau, whereas M_-^{sngl} deviates from the plateau. The deviation becomes visible at $z/a \sim 18$ for $s\bar{s}$ and ~ 20 for $c\bar{c}$. Thus, for our calculations, one can cleanly define the effective correlators [Eq. (B7)] till $z/a < 18$ for $s\bar{s}$ and till $z/a < 20$ for $c\bar{c}$. We also performed a similar study for the $s\bar{c}$ sector and find that the deviation is visible only at $z/a \sim 20$. For positive parity states the amplitudes are smaller than that for the negative parity states, and the effect of the periodic boundary condition is slightly larger. Thus, to be conservative, we apply our procedure for separating the contributions of the positive and negative parities only up to $z/a < 15$.

APPENDIX C: SUMMARY OF SCREENING MASSES

The screening masses determined by fitting the corresponding correlators with the corner-wall sources are summarized in Tables V, VI and VII for the $s\bar{s}$, $s\bar{c}$ and $c\bar{c}$ mesons, respectively. The first and second parentheses give the statistical and systematic errors. The former is estimated from a bootstrap analysis for each fit and the latter gives the systematic ambiguity arising from the variation of the fit range.

TABLE V. Numerical values of the screening masses, in GeV, for the $s\bar{s}$ sector at different temperatures. The first and second parentheses indicate the statistical and systematic errors, respectively.

T [MeV]	0^{-+}	0^{++}	1^{--}	1^{++}
138.2	0.69572(18)(35)	1.0542(40)(96)	1.0469(13)(29)	1.3766(83)(50)
143.3	0.70202(13)(4)	1.041(2)(12)	1.0565(8)(49)	1.343(4)(16)
149.0	0.70997(18)(39)	1.016(2)(17)	1.0618(11)(67)	1.325(5)(23)
153.5	0.71691(20)(33)	1.0115(17)(97)	1.0719(9)(47)	1.300(3)(19)
158.0	0.72777(21)(48)	1.0010(15)(71)	1.0852(9)(51)	1.286(2)(19)
164.3	0.74406(18)(62)	0.9754(12)(64)	1.0982(6)(55)	1.273(2)(20)
167.5	0.75755(34)(67)	0.9715(15)(78)	1.1146(14)(66)	1.273(2)(16)
170.8	0.76538(28)(27)	0.9687(6)(51)	1.1221(10)(67)	1.268(1)(12)
175.8	0.79145(40)(36)	0.9690(11)(26)	1.1475(9)(54)	1.2742(20)(89)
182.6	0.81736(51)(49)	0.9717(8)(59)	1.1673(9)(69)	1.276(1)(16)
189.6	0.8508(5)(11)	0.9834(9)(32)	1.2058(14)(69)	1.2857(20)(85)
196.9	0.8912(5)(11)	1.0034(6)(39)	1.2387(8)(50)	1.3096(14)(85)
210.2	0.9694(5)(11)	1.0474(6)(33)	1.3123(8)(32)	1.3611(10)(61)
220.2	1.0381(6)(12)	1.0979(7)(23)	1.3709(8)(31)	1.4077(8)(51)
247.9	1.23211(58)(73)	1.2689(5)(10)	1.5468(8)(41)	1.5671(9)(49)
297.5	1.5862(30)(17)	1.5969(31)(13)	1.8787(32)(35)	1.8855(34)(40)
371.9	2.1069(23)(35)	2.1150(23)(50)	2.3695(40)(28)	2.3719(41)(29)
495.8	2.9102(40)(55)	2.9181(24)(37)	3.1589(27)(47)	3.1605(27)(51)
743.7	4.512(6)(13)	4.5233(55)(67)	4.7677(45)(70)	4.7674(45)(72)

TABLE VI. Same as Table V, but for the $s\bar{c}$ sector.

T [MeV]	0^{-+}	0^{++}	1^{--}	1^{++}
138.2	1.97625(26)(97)	2.326(3)(10)	2.1176(5)(13)	2.451(8)(14)
143.3	1.97997(17)(81)	2.293(2)(10)	2.12105(47)(83)	2.4255(53)(97)
149.0	1.98459(28)(54)	2.2789(25)(72)	2.12494(46)(58)	2.405(3)(11)
153.5	1.98708(14)(67)	2.2815(18)(42)	2.12906(51)(86)	2.3936(34)(89)
158.0	1.99315(27)(88)	2.2585(20)(45)	2.13648(37)(64)	2.3783(27)(71)
164.3	2.0029(1)(10)	2.2484(12)(40)	2.14577(47)(64)	2.3611(21)(67)
167.5	2.00951(38)(46)	2.2410(18)(38)	2.1554(6)(12)	2.3647(27)(63)
170.8	2.0122(2)(11)	2.2315(9)(33)	2.15700(44)(50)	2.3495(18)(47)
175.8	2.02757(33)(98)	2.2309(14)(19)	2.17614(59)(69)	2.3494(19)(59)
182.6	2.0403(2)(14)	2.2260(9)(29)	2.18684(51)(96)	2.3467(13)(60)
189.6	2.0582(4)(11)	2.2205(8)(12)	2.20748(75)(87)	2.3450(15)(32)
196.9	2.0784(3)(20)	2.2177(7)(18)	2.2269(5)(20)	2.3430(8)(35)
210.2	2.1189(3)(18)	2.2361(5)(16)	2.2740(4)(23)	2.3715(7)(11)
220.2	2.1531(3)(19)	2.2534(5)(14)	2.3103(4)(15)	2.3889(7)(19)
247.9	2.2553(4)(31)	2.3251(3)(21)	2.4160(5)(17)	2.4696(5)(10)
297.5	2.4624(12)(9)	2.5057(10)(20)	2.6368(18)(24)	2.6676(18)(35)
371.9	2.7942(15)(35)	2.8171(14)(38)	2.9782(20)(25)	2.9936(21)(24)
495.8	3.4036(20)(54)	3.4162(21)(50)	3.6043(22)(67)	3.6107(22)(66)
743.7	4.8049(39)(92)	4.8100(41)(93)	5.0251(42)(97)	5.0276(43)(98)

TABLE VII.   Same as Table V, but for the $c\bar{c}$ sector.

T [MeV]	0^{-+}	0^{++}	1^{--}	1^{++}
138.2	2.97844(9)(27)	3.406(9)(21)	3.08523(20)(33)	3.474(11)(23)
143.3	2.98062(7)(31)	3.398(5)(13)	3.08777(18)(34)	3.487(9)(19)
149.0	2.98302(9)(50)	3.392(5)(13)	3.08999(16)(70)	3.467(6)(17)
153.5	2.98150(10)(41)	3.377(3)(14)	3.08871(13)(67)	3.452(7)(15)
158.0	2.98418(8)(60)	3.366(4)(12)	3.09144(16)(85)	3.448(5)(16)
164.3	2.98748(7)(61)	3.352(2)(10)	3.09518(16)(84)	3.419(4)(14)
167.5	2.98746(13)(51)	3.3444(31)(66)	3.09543(21)(40)	3.4205(61)(91)
170.8	2.98641(8)(54)	3.3405(21)(95)	3.09487(13)(84)	3.414(2)(11)
175.8	2.99113(12)(51)	3.3468(28)(84)	3.10050(21)(71)	3.4108(38)(72)
182.6	2.99398(12)(73)	3.3323(21)(75)	3.10473(18)(87)	3.394(2)(10)
189.6	2.99766(14)(63)	3.3231(16)(84)	3.10977(23)(85)	3.3857(21)(75)
196.9	3.00230(14)(87)	3.3031(14)(56)	3.1154(2)(12)	3.3657(18)(76)
210.2	3.0156(1)(10)	3.2975(9)(40)	3.1321(2)(12)	3.3669(14)(49)
220.2	3.0284(1)(11)	3.2914(8)(35)	3.1474(2)(15)	3.3644(9)(40)
247.9	3.0706(1)(14)	3.3016(6)(29)	3.1959(2)(20)	3.3776(10)(37)
297.5	3.17340(62)(79)	3.3635(14)(40)	3.3126(7)(16)	3.4564(20)(38)
371.9	3.3747(7)(31)	3.5109(10)(35)	3.5309(9)(31)	3.6288(12)(38)
495.8	3.8299(14)(67)	3.9185(19)(60)	4.0168(18)(66)	4.0725(27)(49)
743.7	5.044(5)(15)	5.100(3)(10)	5.2768(36)(82)	5.2991(39)(83)

---

[1] T. Bhattacharya, M. I. Buchoff, N. H. Christ, H.-T. Ding, R. Gupta *et al.*, Phys. Rev. Lett. **113**, 082001 (2014).

[2] A. Bazavov, H.-T. Ding, P. Hegde, O. Kaczmarek, F. Karsch *et al.*, Phys. Rev. Lett. **111**, 082301 (2013).

[3] P. Petreczky, J. Phys. G **39**, 093002 (2012).

[4] O. Philipsen, Prog. Part. Nucl. Phys. **70**, 55 (2013).

[5] T. Matsui and H. Satz, Phys. Lett. B **178**, 416 (1986).

[6] R. Sharma, I. Vitev, and B.-W. Zhang, Phys. Rev. C **80**, 054902 (2009).

[7] A. Bazavov, H.-T. Ding, P. Hegde, O. Kaczmarek, F. Karsch *et al.*, Phys. Lett. B **737**, 210 (2014).

[8] C. E. Detar and J. B. Kogut, Phys. Rev. Lett. **59**, 399 (1987).

[9] C. E. Detar and J. B. Kogut, Phys. Rev. D **36**, 2828 (1987).

[10] M. Laine and M. Vepsalainen, J. High Energy Phys. 02 (2004) 004.

[11] B. Brandt, A. Francis, M. Laine, and H. Meyer, J. High Energy Phys. 05 (2014) 117.

[12] M. Asakawa, T. Hatsuda, and Y. Nakahara, Prog. Part. Nucl. Phys. **46**, 459 (2001).

[13] I. Wetzorke, F. Karsch, E. Laermann, P. Petreczky, and S. Stickan, Nucl. Phys. B, Proc. Suppl. **106–107**, 510 (2002).

[14] M. Asakawa, T. Hatsuda, and Y. Nakahara, Nucl. Phys. **A715**, 863c (2003).

[15] M. Asakawa and T. Hatsuda, Phys. Rev. Lett. **92**, 012001 (2004).

[16] S. Datta, F. Karsch, P. Petreczky, and I. Wetzorke, Phys. Rev. D **69**, 094507 (2004).

[17] A. Jakovac, P. Petreczky, K. Petrov, and A. Velytsky, Phys. Rev. D **75**, 014506 (2007).

[18] G. Aarts, C. Allton, M. B. Oktay, M. Peardon, and J.-I. Skullerud, Phys. Rev. D **76**, 094513 (2007).

[19] H.-T. Ding, A. Francis, O. Kaczmarek, F. Karsch, H. Satz, and W. Soeldner, Phys. Rev. D **86**, 014509 (2012).

[20] P. Petreczky, Eur. Phys. J. C **62**, 85 (2009).

[21] W. Florkowski and B. L. Friman, Z. Phys. A **347**, 271 (1994).

[22] O. Kaczmarek, E. Laermann, and M. Müller, The thermodynamic and the continuum limit of meson screening masses, *Proc. Sci.*, LATTICE2013 (2014) 150 [arXiv:1311.3889].

[23] R. Gavai, S. Gupta, and R. Lacaze, Phys. Rev. D **78**, 014502 (2008).

[24] D. Banerjee, R. V. Gavai, and S. Gupta, Phys. Rev. D **83**, 074510 (2011).

[25] H. Iida, Y. Maezawa, and K. Yazaki, Hadron properties at finite temperature and density with two-flavor Wilson fermions, *Proc. Sci.*, LATTICE2010 (2010) 189 [arXiv:1012.2044].

[26] M. Cheng, S. Datta, A. Francis, J. van der Heide, C. Jung *et al.*, Eur. Phys. J. C **71**, 1564 (2011).

[27] E. Laermann and F. Pucci, Taste symmetry breaking at finite temperature, Eur. Phys. J. C **72**, 2200 (2012).

[28] F. Karsch, E. Laermann, S. Mukherjee, and P. Petreczky, Phys. Rev. D **85**, 114501 (2012).

[29] E. Follana, Q. Mason, C. Davies, K. Hornbostel, G. P. Lepage, J. Shigemitsu, H. Trottier, and K. Wong (HPQCD and UKQCD Collaborations), Phys. Rev. D **75**, 054502 (2007).

[30] A. Bazavov, T. Bhattacharya, M. Cheng, C. DeTar, H.-T. Ding *et al.*, Phys. Rev. D **85**, 054503 (2012).

[31] C. T. H. Davies, G. C. Donald, R. J. Dowdall, J. Koponen, E. Follana *et al.*, Precision tests of the J/ψ from full lattice QCD: Mass, leptonic width and radiative decay rate to η_c, *Proc. Sci.*, ConfinementX (2012) 288 [arXiv:1301.7203].

[32] A. Bazavov *et al.* (Fermilab Lattice and MILC Collaborations), Charmed and strange pseudoscalar meson decay constants from HISQ simulations, *Proc. Sci.*, LATTICE2013 (2014) 405 [arXiv:1312.0149].

[33] Y. Maezawa, A. Bazavov, F. Karsch, P. Petreczky, and S. Mukherjee, Meson screening masses at finite temperature with Highly Improved Staggered Quarks, *Proc. Sci.*, LATTICE2013 (2014) 149 [arXiv:1312.4375].

[34] A. Bazavov, F. Karsch, Y. Maezawa, S. Mukherjee, and P. Petreczky, J. Phys. Conf. Ser. **535**, 012031 (2014).

[35] R. Altmeyer, K.D. Born, M. Göckeler, E. Laermann, and G. Schierholz (MT(c) Collaboration), Nucl. Phys. **B389**, 445 (1993).

[36] G. P. Lepage, B. Clark, C. T. H. Davies, K. Hornbostel, P. B. Mackenzie, C. Morningstar, and H. Trottier, Nucl. Phys. B, Proc. Suppl. **106–107**, 12 (2002).

[37] L. Levkova and C. DeTar, Phys. Rev. D **83**, 074504 (2011).

[38] A. Bazavov *et al.* (HotQCD Collaboration), Phys. Rev. D **86**, 034509 (2012).

[39] A. Bazavov *et al.* (HotQCD Collaboration), Phys. Rev. D **90**, 094503 (2014).

[40] J. Beringer *et al.* (Particle Data Group), Phys. Rev. D **86**, 010001 (2012).

[41] C. Davies, C. McNeile, K. Wong, E. Follana, R. Horgan, K. Hornbostel, G. P. Lepage, J. Shigemitsu, and H. Trottier, Phys. Rev. Lett. **104**, 132003 (2010).

[42] K.-l. Wang, Y.-x. Liu, L. Chang, C. D. Roberts, and S. M. Schmidt, Phys. Rev. D **87**, 074038 (2013).

[43] G. Boyd, S. Gupta, F. Karsch, and E. Laermann, Z. Phys. C **64**, 331 (1994).

[44] S. Mukherjee, Screening of light mesons and charmonia at high temperature, Nucl. Phys. **A820**, 283c (2009).

[45] S. Chatterjee, R. Godbole, and S. Gupta, Strange freezeout, Phys. Lett. B **727**, 554 (2013).